Supplementary Information

Water-Responsive Molecule Realizes Stable Ah-Scale Zn–I_2 Pouch Cells with High Zn Utilization

Yiyang Hu,‡[a] Shao-Jian Zhang,‡[a] Han Wu,[a] Qianru Chen,[a] Pengfang Zhang,[b] Junnan Hao,*[a] Shi-Zhang Qiao*[a]

[a] School of Chemical Engineering, The University of Adelaide, Adelaide, SA 5005, Australia

[b] School of Chemistry and Chemical Engineering, Liaocheng University, Liaocheng 252000, P. R. China

*Corresponding author: junnan.hao@adelaide.edu.au, s.qiao@adelaide.edu.au

‡ These authors contributed equally to this work.

1. Experimental Procedures

1.1 Chemical reagent

Ectoine (Ect, $C_6H_{10}N_2O_2$, ⩾98.0%) was purchased from Beijing InnoChem Science & Technology Co., Ltd. Zinc sulfate heptahydrate ($ZnSO_4·7H_2O$, ⩾99.0%), iodine (I_2, ⩾99.99%), sodium iodide (NaI, ⩾ 99.0%), potassium iodide (KI, ⩾ 99.0%), sodium sulfate ($Na_2SO_4·7H_2O$, ⩾ 99.0%) and polytetrafluoroethylene (PTFE) aqueous dispersion (60 wt.% solid content) were purchased from Sigma-Aldrich. Zn foils, Cu foils, Ketjenblack (KB), titanium mesh (100 mesh) were provided by Canrd New Energy Technology Co., Ltd. The glass fiber (GF/A 2916, Olegeeino) was provided by Chongqing Olegee Technology Co., Ltd.

1.2 Electrolyte preparation

The base $ZnSO_4$ electrolyte was prepared by dissolving $ZnSO_4·7H_2O$ in deionized water with the concentrations of 2 M. Ect electrolytes with varying concentrations (0.5 wt.%, 5 wt.%, 10 wt.%, 20 wt.%, and 35 wt.%, calculated based on electrolyte mass) were prepared by adding the corresponding amount of Ect to 2 M $ZnSO_4$ electrolyte. The optimized Ect concentration was determined to be 5 wt.%.

1.3 Preparation of KB–I_2 electrodes

KB and I_2 were mixed at a 3:7 mass ratio and manually ground for 10 min. The mixture was then hermetically sealed in a quartz tube and subjected to thermal treatment at 80 °C for 6 h, resulting in the formation of KB–I_2 composite powder. For KB–I_2 electrode preparation, the KB–I_2 composite powder was blended with KB and PTFE in a mass ratio of 8:1:1. The mixture was then compressed onto a Ti mesh and dried at 40 °C for 2 h to eliminate any residual solvents. For Zn–I_2 coin cells, the I_2 loading in the cathodes was controlled within the range of 7–10 mg_{iodine} cm^{-2}, while for Zn–I_2 pouch cells, a higher I_2 loading of 19–20 mg_{iodine} cm^{-2} was employed. Notably, all reported I_2 loadings refer to the amount calculated per single side of the cathode.

1.4 Electrochemical measurements

To evaluate the CE of the Zn anode, a Zn||Cu asymmetric cell was assembled. During the test, Zn was plated onto a Cu foil (19 mm in diameter) at a predetermined current density, followed by stripping at the same current density until the voltage reached 0.8 V. To investigate the stability of the Zn plating/stripping process, a Zn||Zn symmetric cell was assembled using two Zn foils (16 mm in diameter), with glass fibers (19 mm in diameter) as a separator. For Zn–I_2 coin cells, KB–I_2 electrodes were paired with Zn foil and assembled as CR2032 coin cells, where glass fibers served as

the separator and either pure 2 M $ZnSO_4$ or Ect electrolyte was used as the electrolyte. GCD measurements of Zn–I_2 coin cells were conducted using a battery test system (CT-4008T, Neware, China) within a voltage range of 0.6–1.6 V. All current densities were calculated based on the mass of I_2. CV measurements were performed using an electrochemical workstation (CHI660E, Chenhua, China). To evaluate Zn plating/stripping under 50% ZUR, Zn||Cu asymmetric cells were assembled using Zn foils (16 mm in diameter) and Cu foils (19 mm in diameter). Prior to cycling, the Cu electrodes were pre-activated at 2 mA cm^{-2} and 1 mAh cm^{-2} for 20 cycles. Subsequently, 4 mAh cm^{-2} of Zn was pre-deposited onto the Cu foil at a current density of 2 mA cm^{-2}. During subsequent cycling, the Zn||Cu asymmetric cells with Zn pre-deposited Cu electrodes were cycled at 2 mA cm^{-2} and 2 mAh cm^{-2}. For Zn plating/stripping under 70% ZUR, after pre-depositing the same amount of Zn, the Zn||Cu asymmetric cells were cycled at 2 mA cm^{-2} and 2.8 mAh cm^{-2}.

The single-layer Zn–I_2 pouch cells with limited Zn supply were assembled by stacking one double-side coated KB–I_2 electrodes (70 × 80 mm) with two Zn-plated Cu foils (72 × 82 mm). The Zn-plated Cu foils (Zn@Cu) were prepared in a galvanic bath filled with Ect electrolyte, where Zn deposition was carried out at a current density of 6.6 mA cm^{-2} to achieve the required Zn capacity. Glass fibers were used as the separator, while 2 M $ZnSO_4$ (base) or Ect electrolyte served as the electrolyte. The KB–I_2 electrodes for pouch cells were fabricated by pressing a mixture of KB–I_2, KB, and PTFE onto both sides of a titanium mesh current collector. The electrochemical performance of the Zn–I_2 pouch cells was evaluated within a voltage range of 0.6–1.6 V using the battery test system (CT-4008T, Netware, Shenzhen, China) under the ambient conditions.

The multi-layer Zn–I_2 pouch cells were assembled by stacking two double-sided KB–I_2 cathodes (80 × 90 mm) with three Zn@Cu anodes (82 × 92 mm, comprising two single-sided Zn@Cu and one double-sided Zn@Cu anode). Glass fiber and the Ect electrolyte served as the separators and electrolytes, respectively. The electrochemical performance was measured within the voltage range of 0.6–1.6 V using the same battery test system under ambient conditions.

The self-discharge rate was evaluated using the following protocol: (1) Each cell was first charged galvanostatically at 1 C to 1.6 V. The charge capacity was recorded as C_1, and the cell voltage at the beginning of the rest period was recorded as V_1. (2) The cell was then rested under open-circuit conditions for a predefined duration (0.5, 1, 2, 6, 12, 24, and 48 h). The cell voltage at the end of the rest period was recorded as V_2. (3) After the rest period, the cell was discharged galvanostatically at 1 C to 0.6 V, and the discharge capacity was recorded as C_2. (4) To minimize potential bias arising from interfacial instability after prolonged resting, the cell was further cycled for 5 cycles at 2 C

between 0.6 and 1.6 V before proceeding to the next self-discharge interval. Based on these measurements, the self-discharge rate was defined as C_2/C_1, and the voltage drop during the rest period was calculated as V_1-V_2.

2. Characterization Techniques

XRD patterns were collected using a Rigaku Ultima IV X-ray diffractometer with Cu Kα radiation (λ = 1.5418 Å). Field emission scanning electron microscopy (FE-SEM, Hitachi SU 8010) was used to observe sample morphology, while EDS was employed for elemental analysis. To examine the cross-sectional morphology of Zn, Leica EM TIC 3X ion beam milling technology was used to expose the sample cross-sections. UV-Vis spectroscopy was conducted on a Shimadzu UV-2600i spectrophotometer. XPS measurements were performed using a Thermo Fisher Scientific K-Alpha X-ray photoelectron spectrometer with Al Kα X-ray source. The binding energies were calibrated against the C–C peak at 284.8 eV. FTIR spectroscopy was recorded on a Nicolet iS50 spectrometer. ^{1}H NMR spectra of the mixed Ect/triiodide solutions were collected on a Bruker AVANCE III 300 MHz spectrometer at 298 K and samples were prepared in 90 vol.% H_2O/10 vol.% D_2O and transferred into NMR tubes.

Raman spectroscopy was conducted using a Renishaw inVia Raman microscope with a 532 nm wavelength laser. *In situ* Raman spectra of electrodes were obtained using a two-electrode Raman cell (Gaoss Union, B002-RM). Zn–I_2 cells were galvanostatically charged and discharged using an electrochemical workstation (CHI660E, Chenhua, China). Raman spectra were collected through the quartz window of the Raman cell using a Raman microscope.

In situ UV–Vis spectroscopy was performed to monitor the dissolution behavior of polyiodides. A custom-designed quartz cell was prepared by adhering KB–I_2 electrodes and Zn anodes to the rough sides of the quartz cell. The cell was then filled with 3 mL of electrolyte (base or Ect). GCD cycling of the quartz battery was conducted using an electrochemical workstation (CHI660E, Chenhua, China) over a voltage range of 0.6–1.6 V. UV–Vis spectra were collected in real time to monitor the polyiodide dissolution during the cycling process.

In situ differential electrochemical mass spectrometry (DEMS) was conducted on an online DEMS system (HPR-40, Hiden Analytical) to monitor gas evolution during electrochemical processes using a modified DEMS cell. The pressure difference between the electrochemical cell and the vacuum chamber enabled the generated H_2 to be continuously extracted into the vacuum chamber for mass-spectrometric analysis. The working electrode consisted of a 50 nm Au film sputtered onto a PTFE membrane (pore size: 0.02 μm). An Ag/AgCl electrode (Pine Research) and a Pt wire were

used as reference and counter electrodes, respectively. During measurements, linear sweep voltammetry (LSV) was conducted from 0 to −1.2 V (vs. Ag/AgCl) at a scan rate of 5 mV s^{-1} using an electrochemical workstation (CHI660E, Chenhua, Shanghai). Gas species released during the cathodic scan were continuously transferred to the vacuum chamber and analyzed by the mass spectroscopy.

3. Theoretical Calculations

MD simulations were performed using the GROMACS package. The simulations employed the Amber03 force and the TIP3P water model. The systems underwent energy minimization and equilibration under the NPT ensemble, followed by production runs of 10 ns under the canonical ensemble. Temperature coupling to 298 K was achieved using the Nose-Hoover method, and pressure was coupled to 1 atm using the Parrinello-Rahman method. A cutoff scheme of 1.2 nm was applied for non-bonded interactions, and the Particle Mesh Ewald method with a Fourier spacing of 0.1 nm was used for long-range electrostatic interactions. The LINCS algorithm was used to constrain all covalent bonds involving hydrogen atoms. The electrostatic potential was calculated by ORCA package. The structural relaxation, single-point energy calculations, were performed under the B3PLYP-D3/def2-TZVP.

All DFT calculations were performed using the Gaussian 16 software package.[1] Geometry optimizations were carried out at the B3LYP[2]/def2-TZVP[3] level of theory, incorporating Grimme's DFT-D3 dispersion correction[4,5] to account for long-range van der Waals interactions. Default convergence thresholds were employed, with maximum force and displacement criteria set to <0.00045 Hartree/Bohr and <0.0018 Å, respectively. Harmonic vibrational frequency analyses were conducted at the same level of theory to confirm that the optimized structures correspond to true minima on the potential energy surface, as indicated by the absence of imaginary frequencies (v > 0 cm^{-1}). Typically, the conversion from "*+I_5" to "*I_5" represents the adsorption of I_5 species.

To ensure theoretical consistency, single-point energy calculations were performed on the optimized geometries using the same B3LYP/def2-TZVP level. The binding energy (BE) between interacting species was calculated according to the following equation:

$$\mathrm{BE} = E_{\mathrm{complex}} - (E_a + E_b) \qquad \text{(Equation 1)}$$

where $E_{complex}$ is the total energy of the optimized supramolecular complex, and E_a and E_b represent the energies of the isolated components in their optimized geometries.

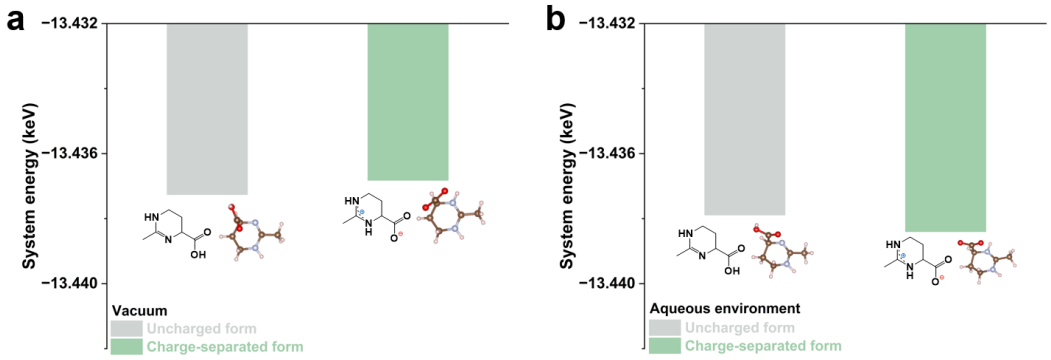

Fig. S1 DFT-calculated energies of Ect in the uncharged and charge-separated states in (a) vacuum and (b) aqueous environment.

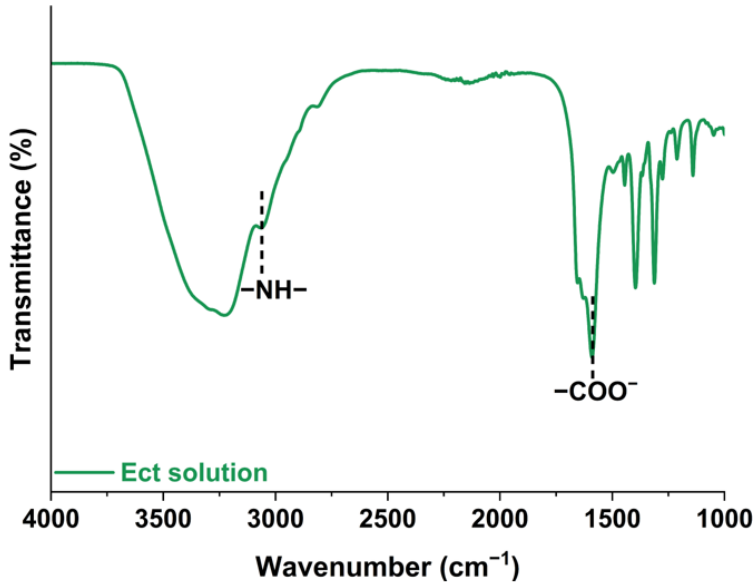

Fig. S2 FTIR spectra of Ect aqueous solution.

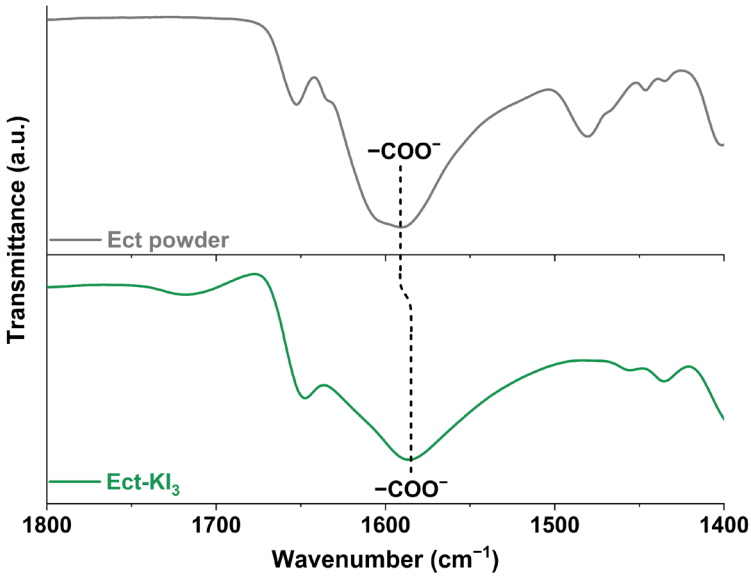

Fig. S3 FTIR spectra of Ect powder and the Ect–KI_3 mixture in the range of 1800–1400 cm^{-1}.

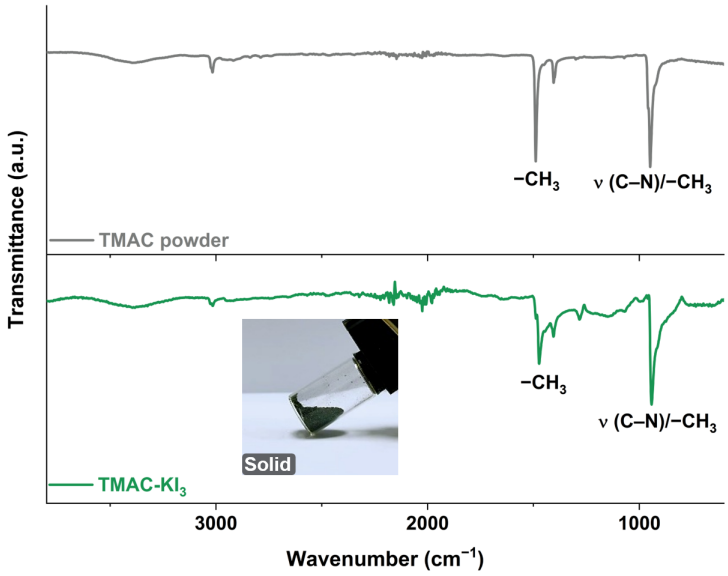

Fig. S4 FTIR spectra of TMAC powder and the TMAC–KI_3 mixture in the range of 3800–600 cm^{-1} (insets: digital photographs of the TMAC–KI_3 mixture after heating to 80 °C).

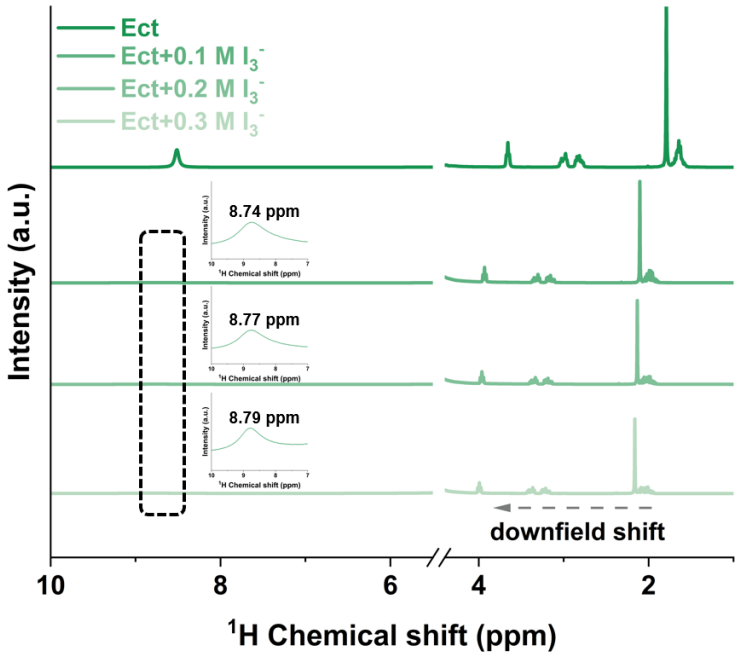

Fig. S5 ^{1}H NMR spectra of Ect solutions with different I_3^- concentrations (insets: expanded view of the ^{1}H chemical shift region from 10 to 7 ppm).

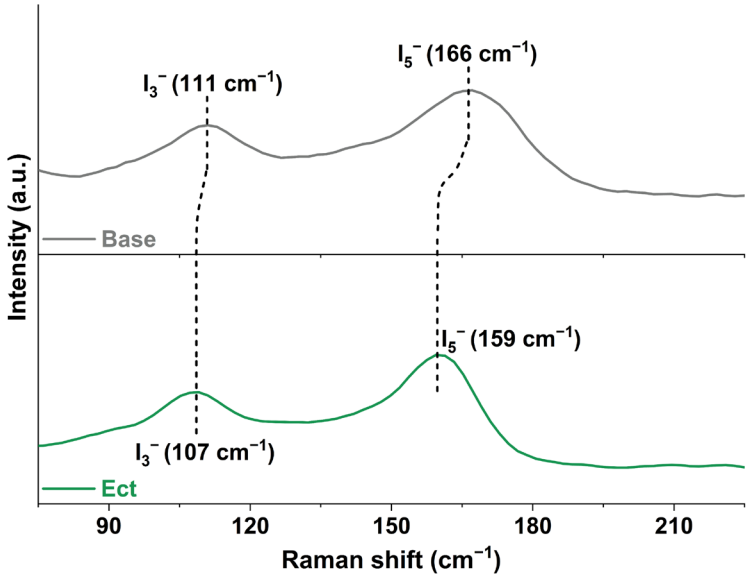

Fig. S6 Ramans spectra of KI_3 and the Ect–KI_3 mixture dissolved in $ZnSO_4$ solution.

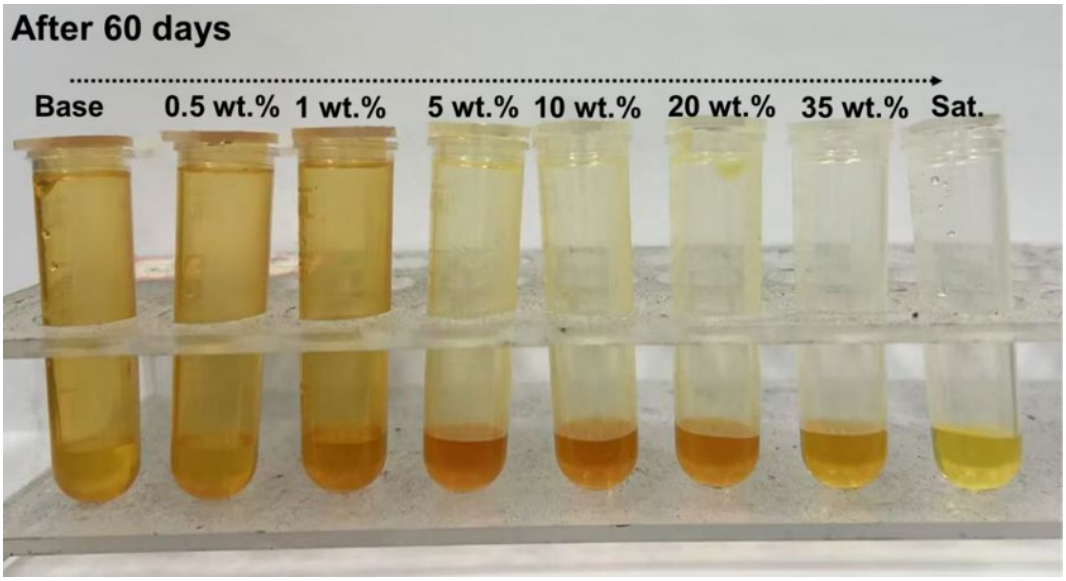

Fig. S7 Digital photograph of mixed solutions containing different concentrations of Ect and I_3^- after 60 days of storage in plastic test tubes.

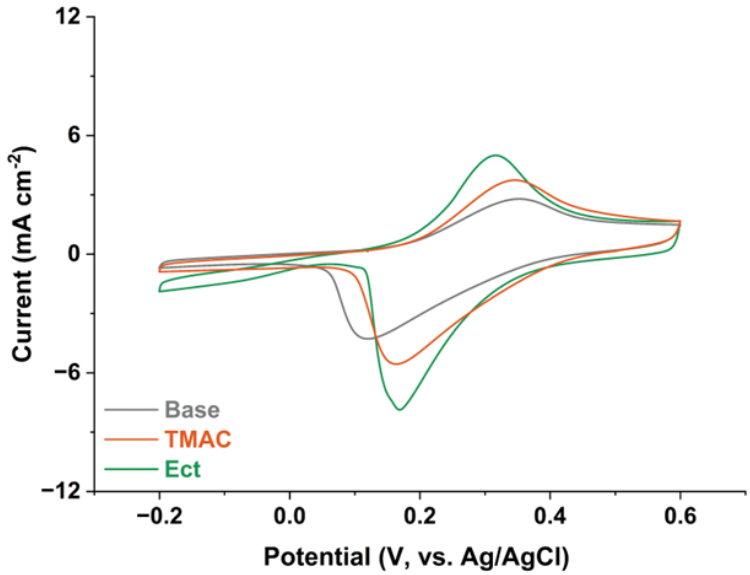

Fig. S8 CV profiles for iodine conversion in base, TMAC and Ect electrolytes at 1 mV s^{-1}

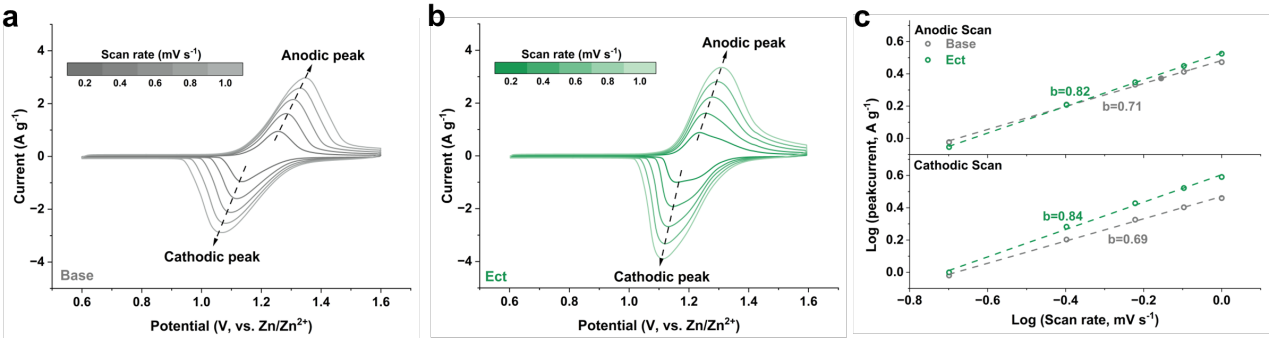

Fig. S9 CV profiles of Zn–I_2 batteries using (a) base and (b) Ect electrolytes at different scan rates. (c) Log(i) vs. log(v) plots of the cathodic (top) and anodic (bottom) peak currents in both electrolytes.

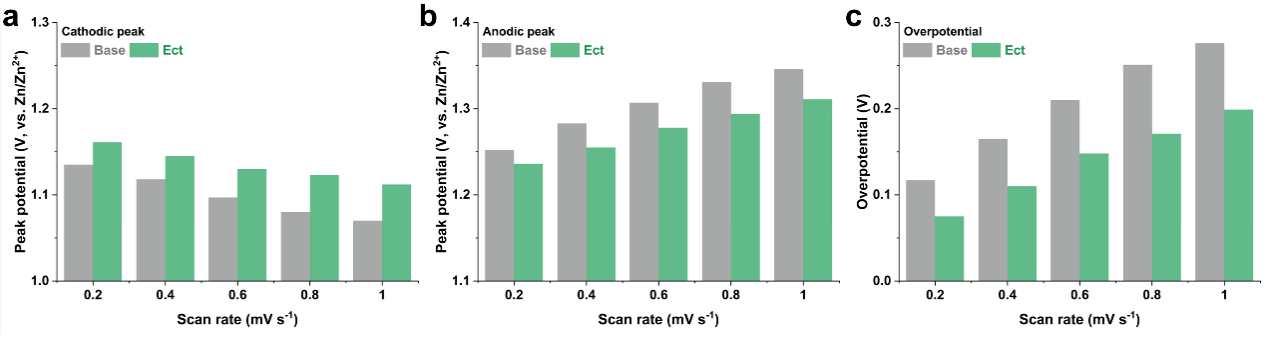

Fig. S10 (a) Cathodic and (b) anodic peak potentials from the CV profiles of Zn–I_2 batteries at different scan rates. (c) Comparison of overpotentials in different electrolytes at various scan rates. Overpotential is defined as the difference between anodic and cathodic peak potentials.

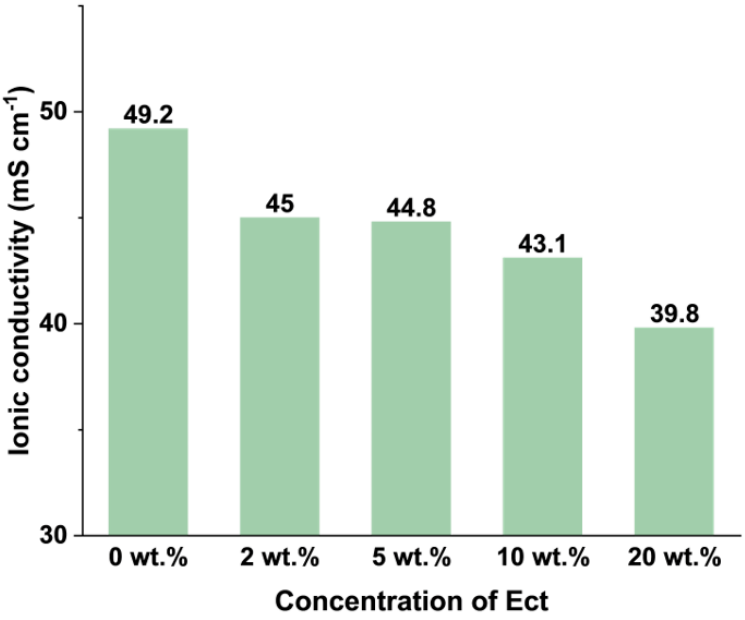

Fig. S11 Ionic conductivities of 2 M $ZnSO_4$ electrolytes with different Ect concentrations.

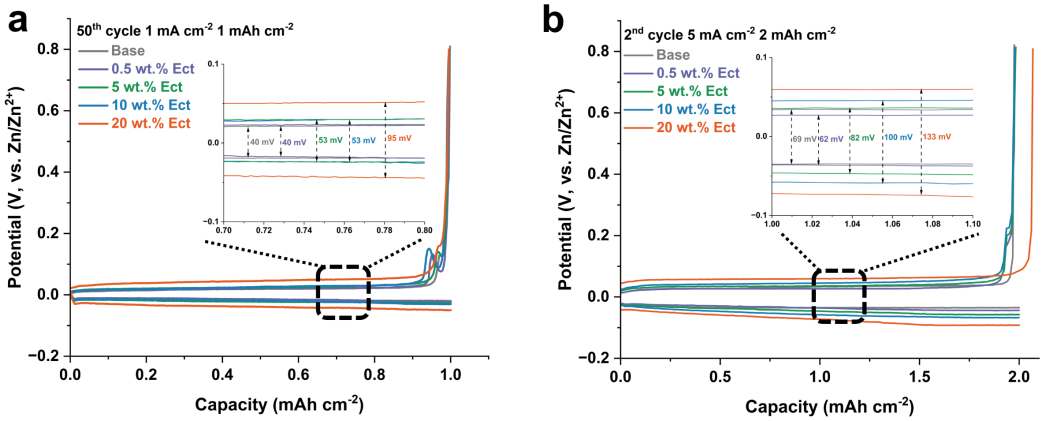

Fig. S12 Zn plating/stripping GCD curves of Zn||Cu cells using electrolytes with different Ect concentrations at: (a) 50th cycle at 1 mA cm^{-2}, 1 mAh cm^{-2}. (b) 2nd cycle at 5 mA cm^{-2}, 2 mAh cm^{-2} (insets: comparison of overpotential from the selected region of the GCD curves).

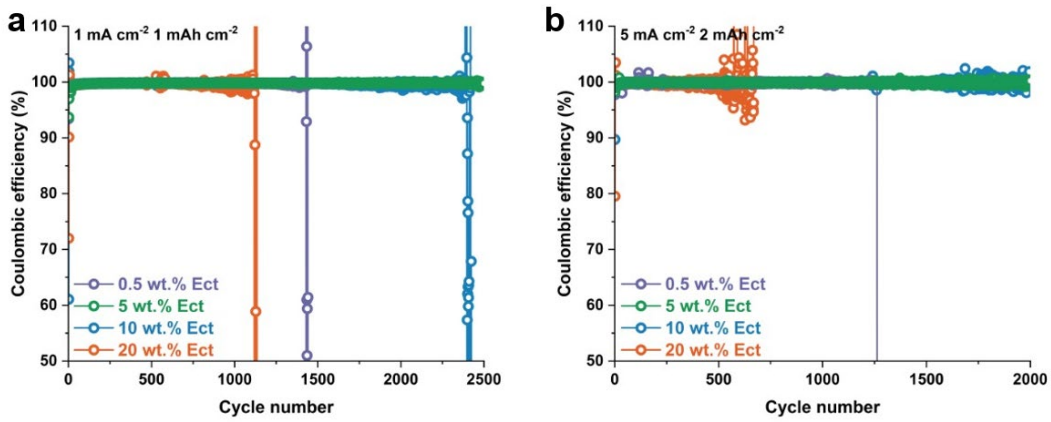

Fig. S13 CEs of Zn||Cu cells using electrolytes with different Ect concentrations at (a) 1 mA cm^{-2}, 1 mAh cm^{-2} and (b) 5 mA cm^{-2}, 2 mAh cm^{-2}.

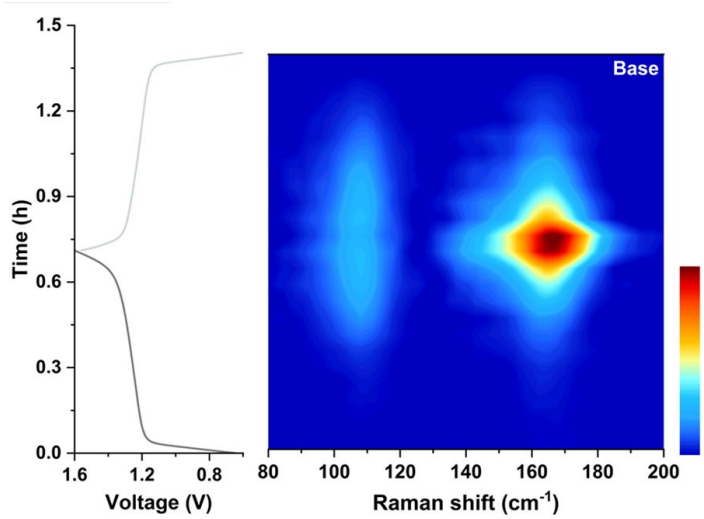

Fig. S14 *In situ* Raman spectra of the Zn–I_2 battery using base electrolyte.

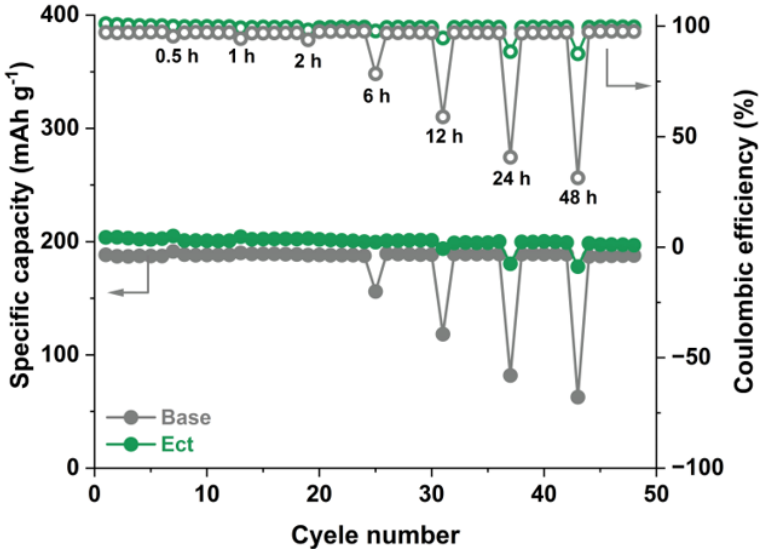

Fig. S15 Self-discharge performance of Zn–I_2 coin cells using base and Ect electrolytes.

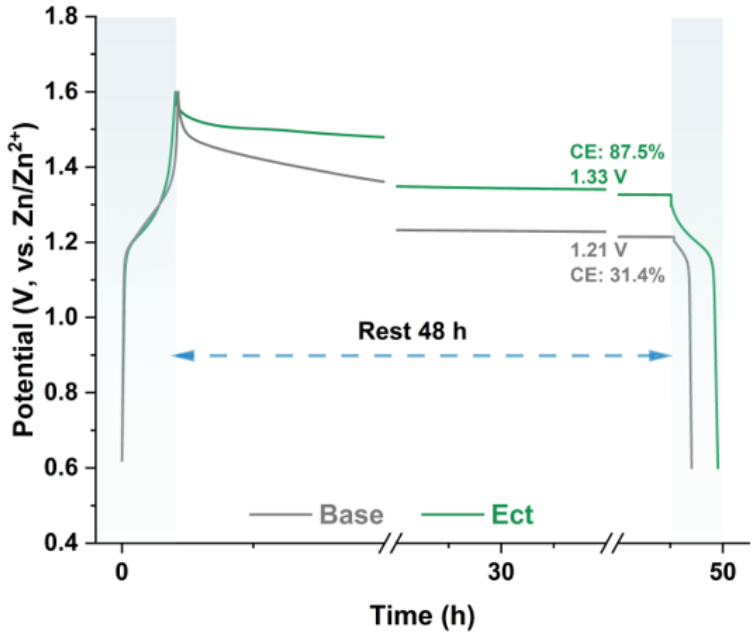

Fig. S16 Self-discharge curves of Zn–I_2 coin cells over 48 h of resting time.

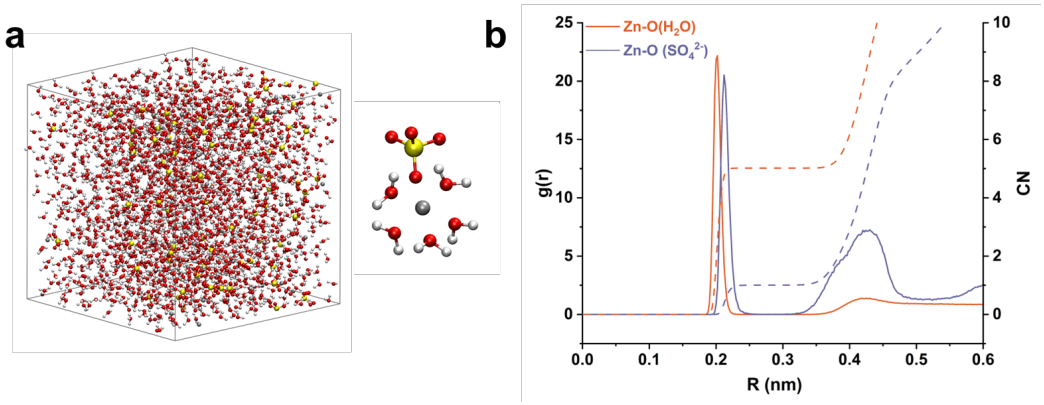

Fig. S17 (a) Snapshot of the base electrolyte obtained from AIMD simulations, with an enlarged view of the Zn^{2+} solvation structure. (b) RDFs for Zn^{2+}–O (H_2O) and Zn^{2+}–O (SO_4^{2-}) collected from AIMD simulations in the base electrolyte.

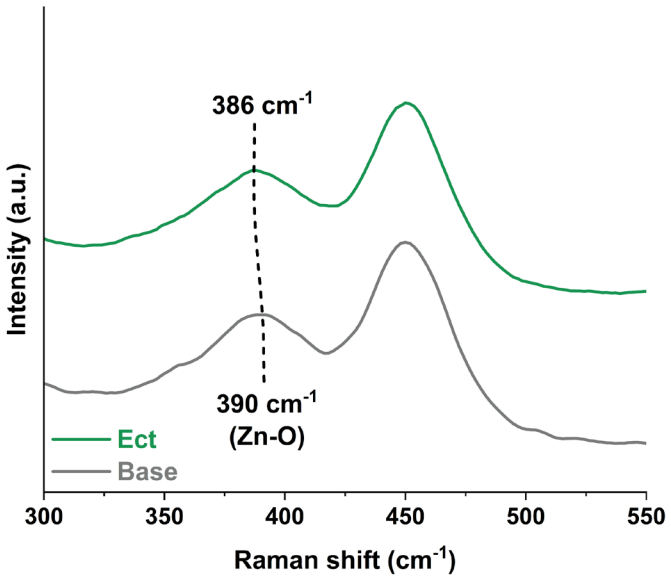

Fig. S18 Raman spectra of the base and Ect electrolytes in the 300–550 cm^{-1} region.

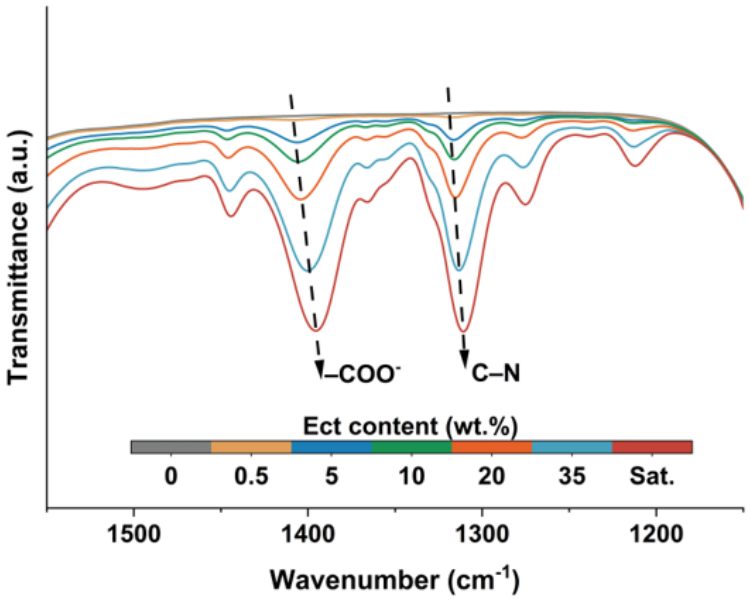

Fig. S19 ATR-FTIR spectra of Ect electrolytes with varying Ect concentrations in the wavenumber range of 1550–1150 cm^{-1}.

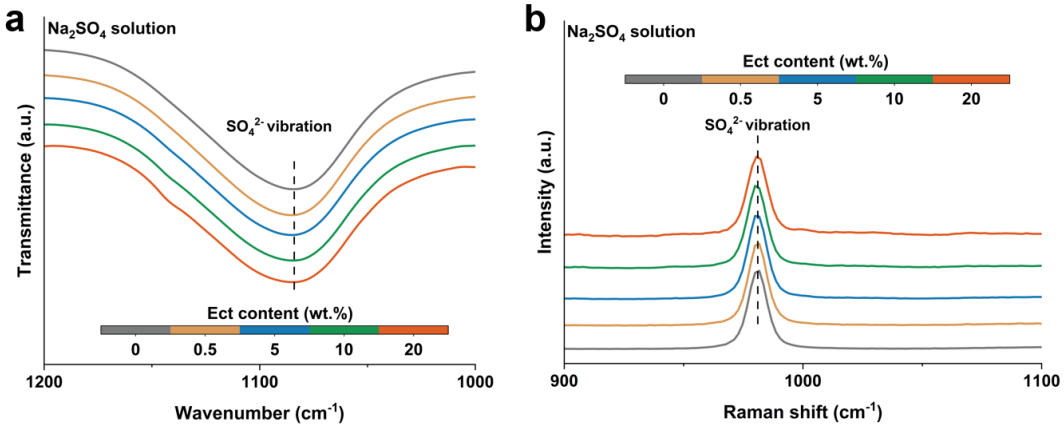

Fig. S20 (a) FTIR spectra and (b) Raman spectra of 2 M Na_2SO_4 solutions containing different concentrations of Ect.

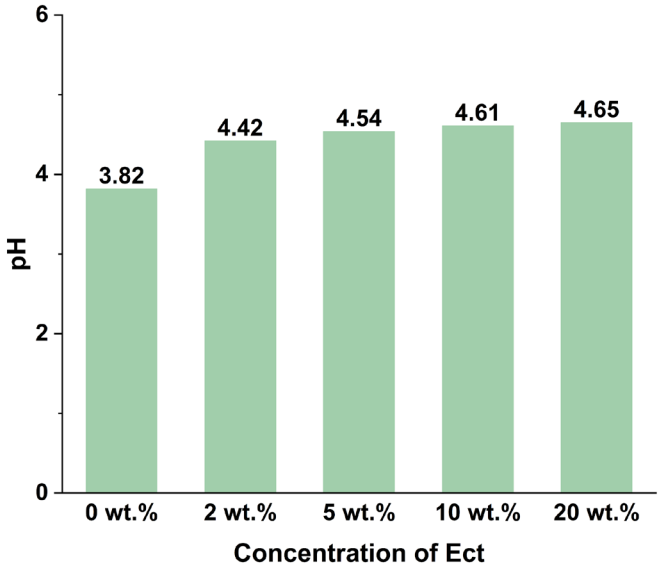

Fig. S21 pH values of 2 M $ZnSO_4$ electrolytes with different concentrations of Ect.

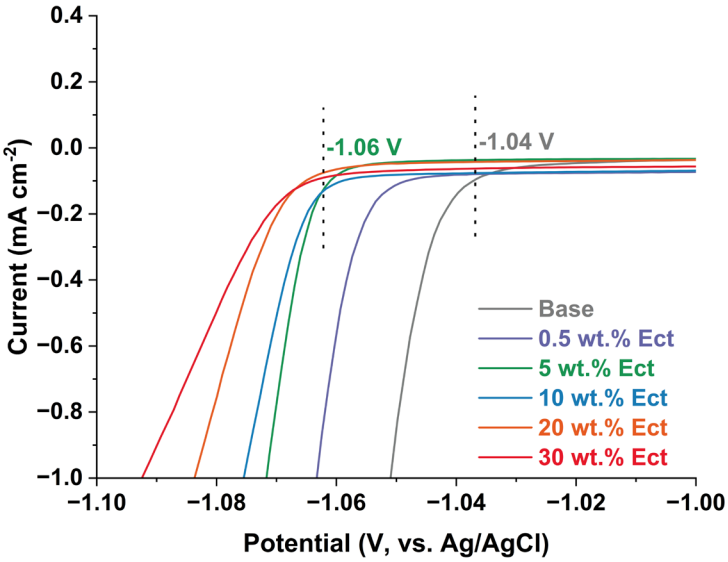

Fig. S22 Electrochemical stability window of electrolytes with varying Ect concentrations at a scan rate of 5 mV s^{-1}.

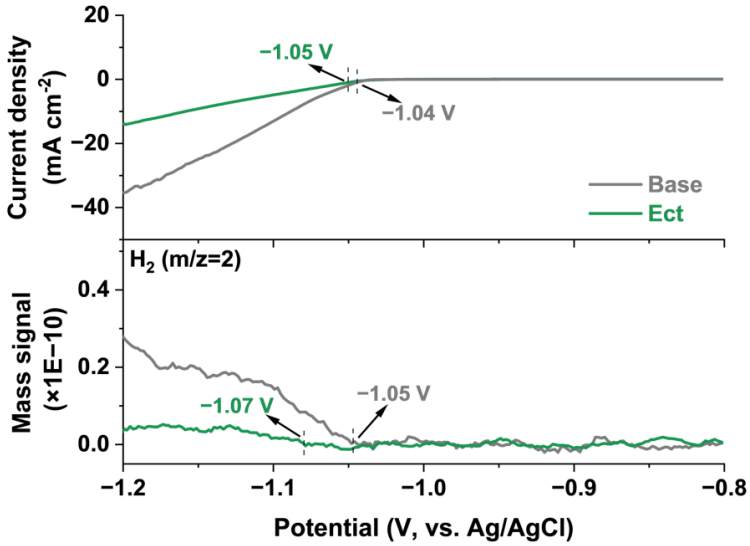

Fig. S23 LSV curves (top) and corresponding *in situ* DEMS mass signal of H_2 (bottom) measured from −0.8 V to −1.2 V (*vs.* Ag/AgCl).

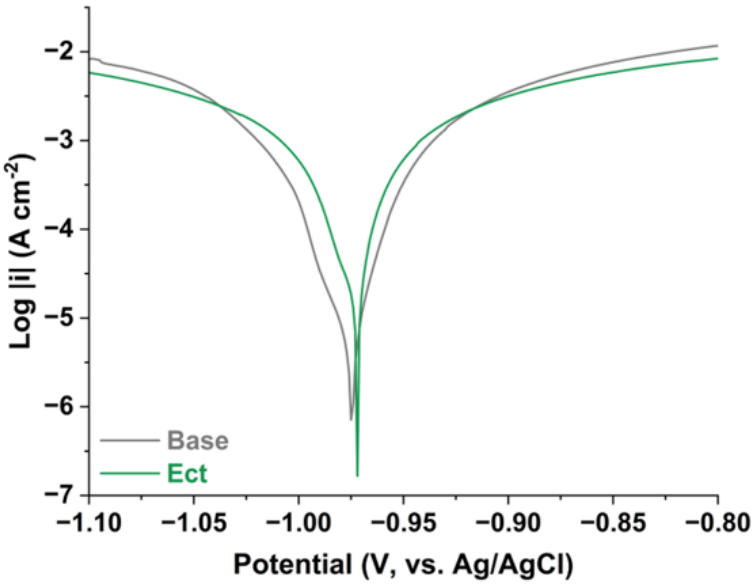

Fig. S24 Tafel plots showing the corrosion behavior of Zn metal in base and Ect electrolytes.

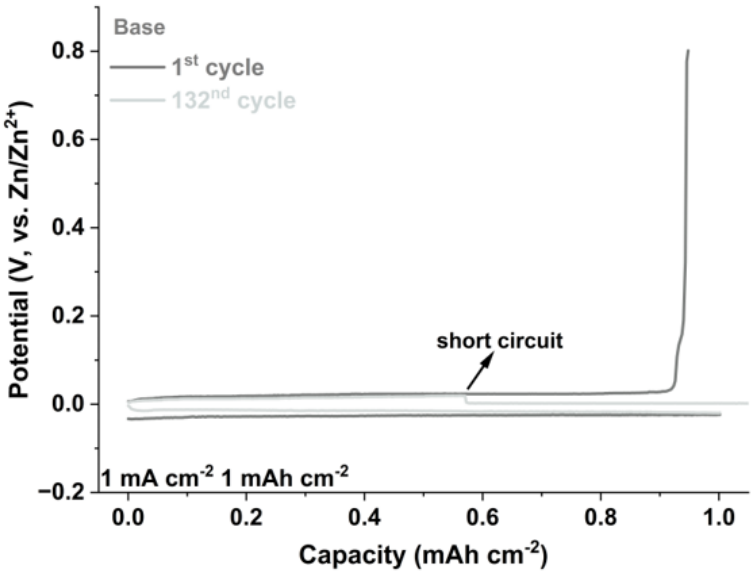

Fig. S25 Zn plating/stripping GCD curves of Zn||Cu asymmetric cells at 1 mA cm^{-2}, 1 mAh cm^{-2} using base electrolyte at 1st and 132nd cycles.

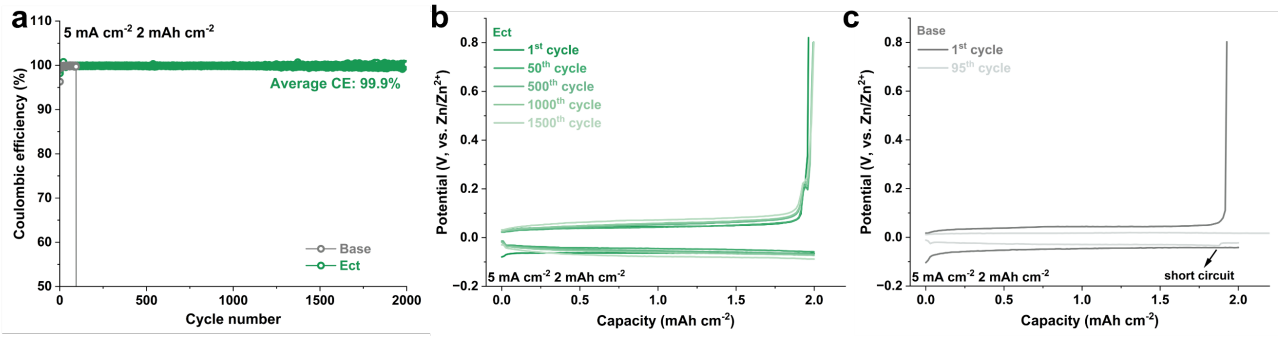

Fig. S26 (a) CEs of Zn||Cu asymmetric cells using base and Ect electrolytes at 5 mA cm^{-2}, 2 mAh cm^{-2}. Zn plating/stripping GCD curves of Zn||Cu cells using (b) Ect and (c) base electrolytes at different cycles.

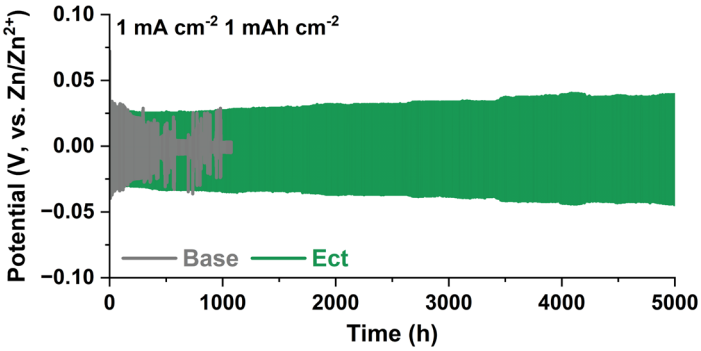

Fig. S27 Comparison of cycling stability and voltage hysteresis of Zn||Zn symmetric cells under different current densities and areal capacities of 1 mA cm^{-2}, 1 mAh cm^{-2}.

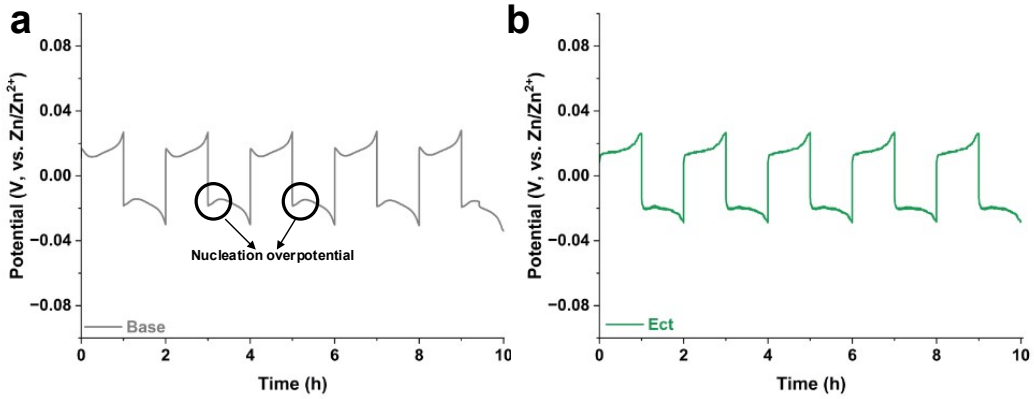

Fig. S28 Overpotential evolution of Zn||Zn symmetric cells using (a) base and (b) Ect electrolyte.

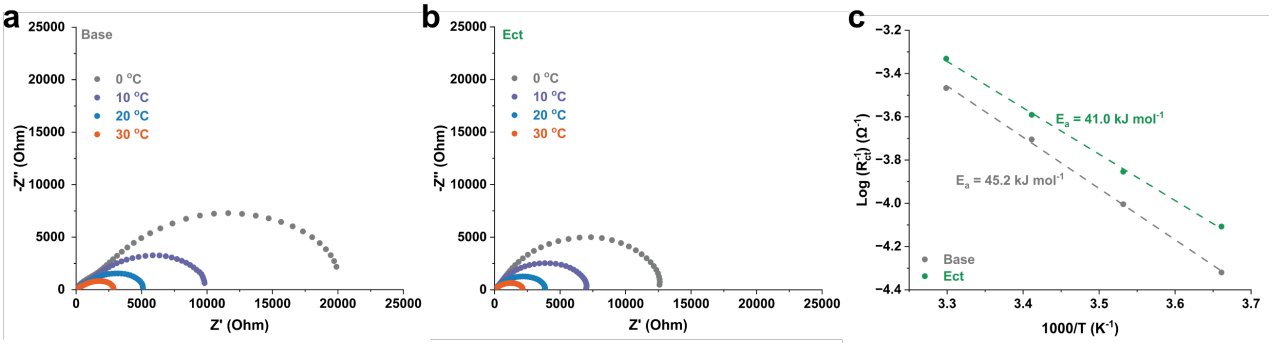

Fig. S29 Nyquist plots of Zn||Zn symmetric cells at different temperatures in (a) base and (b) Ect electrolytes. (c) Corresponding Arrhenius plots and comparison of desolvation energies of Zn||Zn symmetric cells in the two electrolytes.

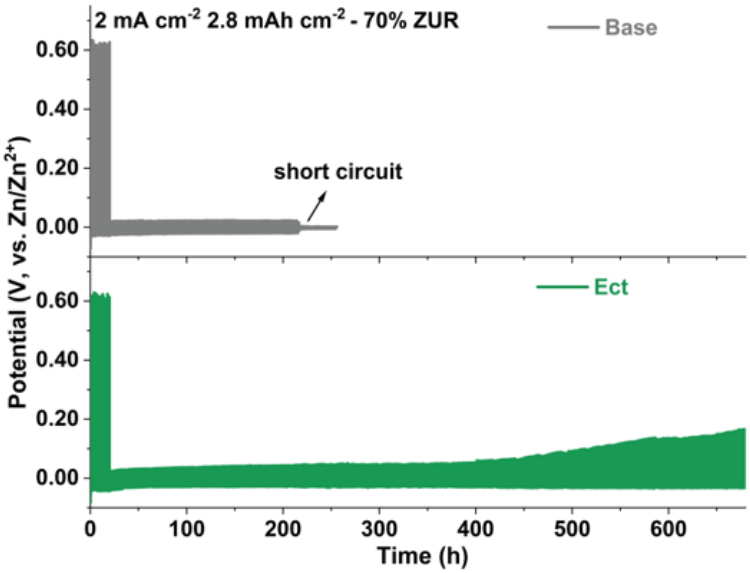

Fig. S30 Galvanostatic Zn plating/stripping in a Zn||Cu asymmetric cell at 2 mA cm^{-2} and 2.8 mAh cm^{-2} under 70% ZUR, with a pre-deposited Zn of 4 mAh cm^{-2}.

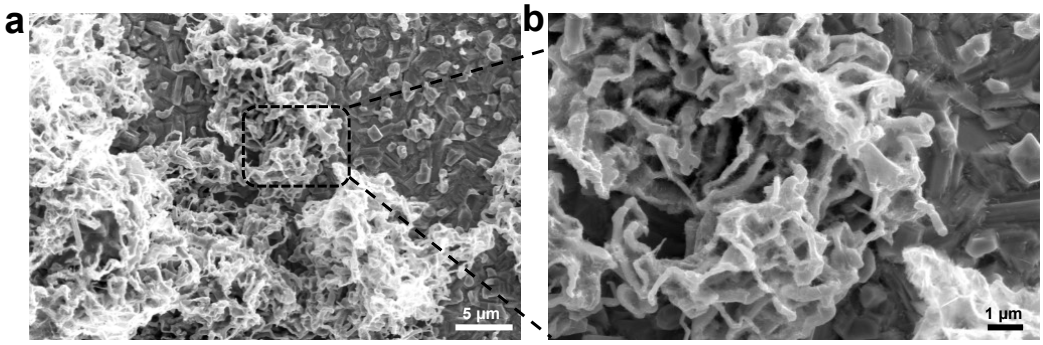

Fig. S31 Top-view SEM images of Zn deposition morphology in base electrolyte at 2 mA cm^{-2} and 4 mAh cm^{-2} at (a) low magnification and (b) high magnification.

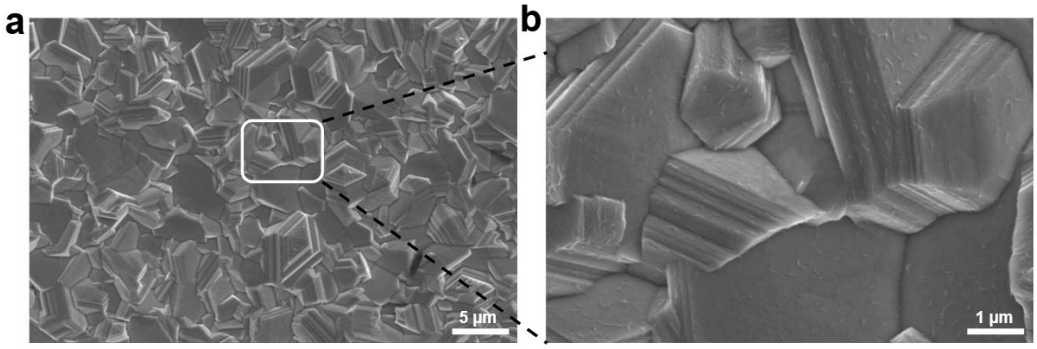

Fig. S32 Top-view SEM images of Zn deposition morphology in Ect electrolyte at 2 mA cm^{-2} and 4 mAh cm^{-2} at (a) low magnification and (b) high magnification.

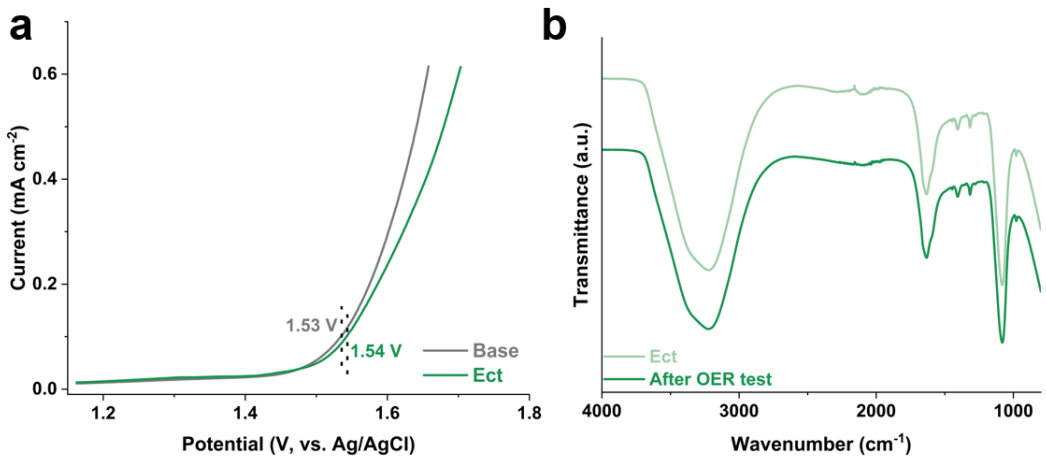

Fig. S33 (a) LSV profiles of the base and Ect electrolytes for oxidation stability evaluation (scan rate: 5 mV s^{-1}). (b) FTIR spectra of the Ect electrolyte collected before and after the anodic stability test.

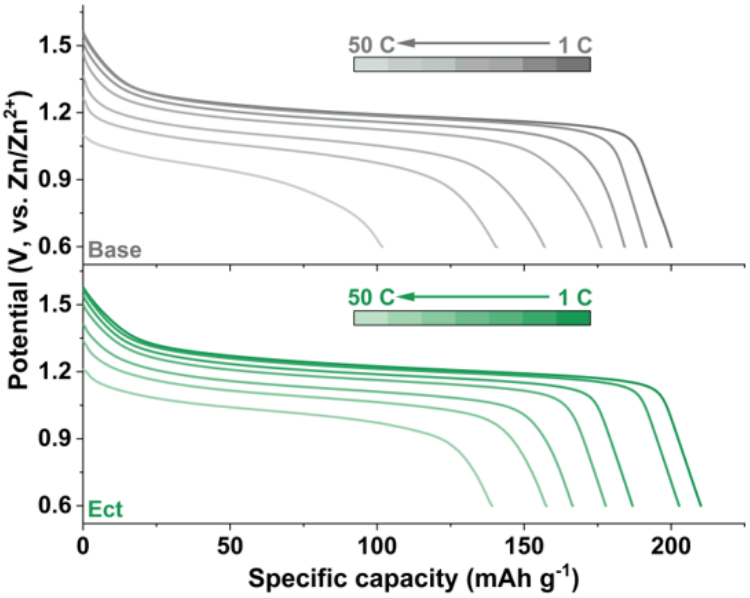

Fig. S34 GCD curves of Zn–I_2 batteries at different current densities.

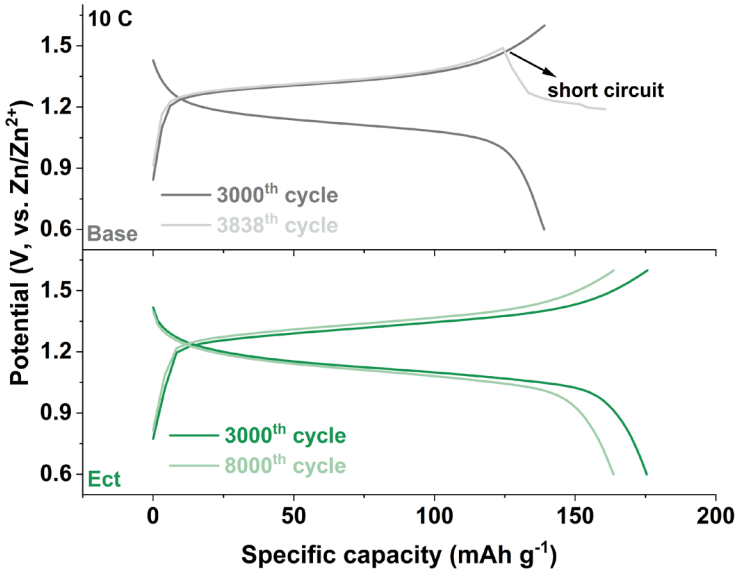

Fig. S35 GCD curves of Zn–I_2 batteries using different electrolytes at 10 C.

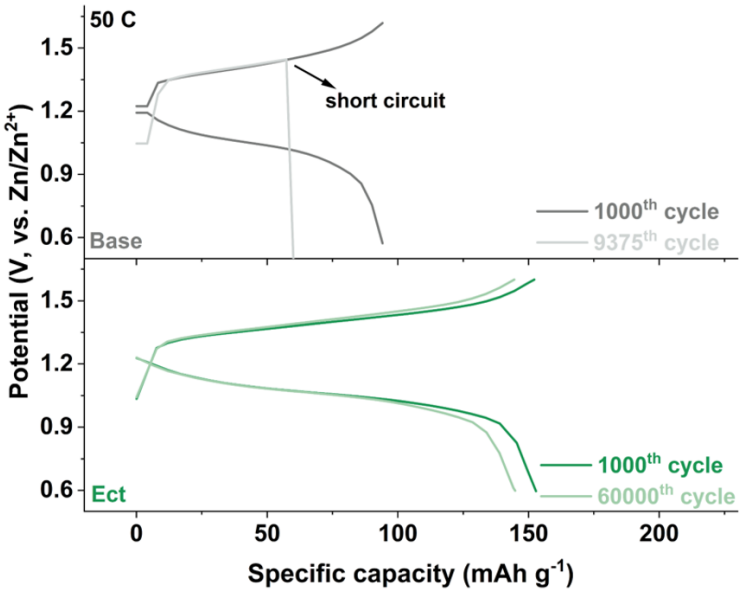

Fig. S36 GCD curves of Zn–I_2 batteries using different electrolytes at 50 C.

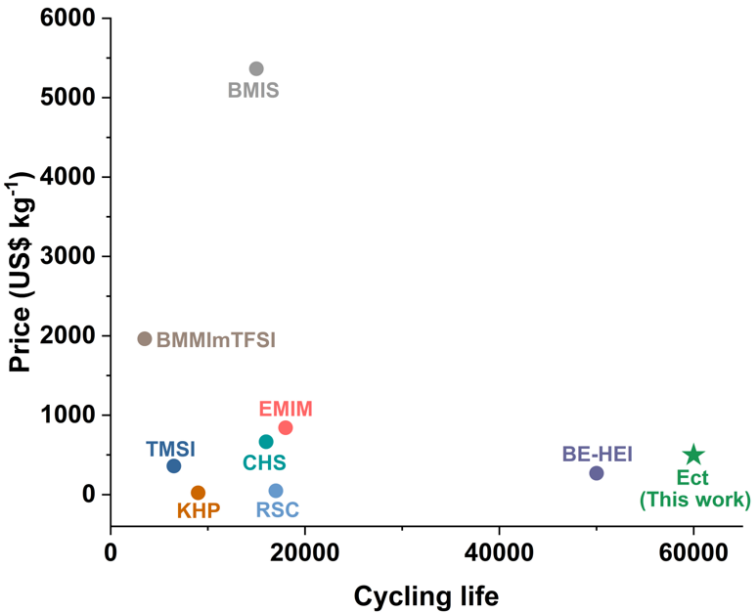

Fig. S37 Comparison of raw-material prices and cycling life of this work with previously reported aqueous Zn–I_2 batteries.

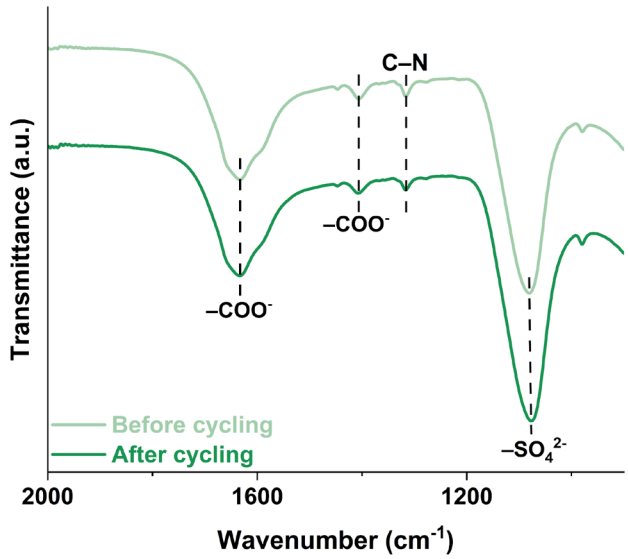

Fig. S38 FTIR spectra of the Ect electrolyte collected before after cycling at 50 C in the wavenumber range of 2000–900 cm^{-1}.

Fig. S39 Digital photograph of the 400 mAh Zn–I_2 pouch cell.

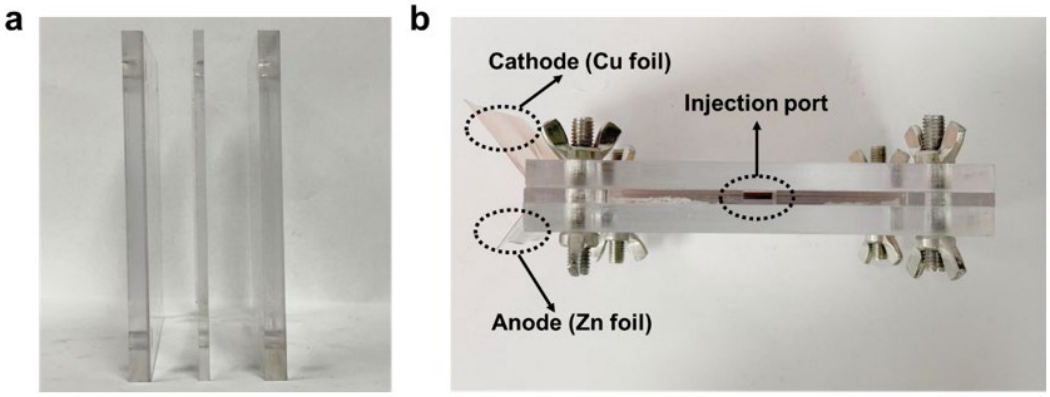

Fig. S40 Digital photograph of the galvanizing bath used for Zn deposition in: (a) disassembled state and (b) assembled state.

Fig. S41 Digital photograph of Zn plated on a Cu foil at a current density of 6.6 mA cm^{-2} in the Ect electrolyte.

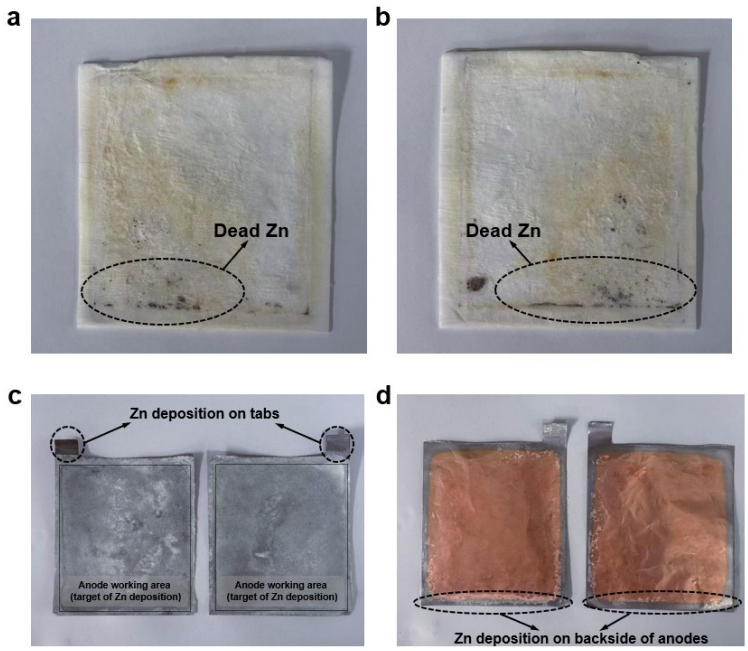

Fig. S42 Digital photographs of (a) front side and (b) back side of glass-fiber separator and (c) front side and (d) back side of the Zn@Cu anode recovered from a disassembled pouch cell (ZUR = 65%) after 1,200 cycles.

Table S1 Comparison of key performance parameters and cycling life of this work with representative Zn–I_2 coin cells reported recently

Strategies	Loading (mg_{iodine} cm^{-2})	Current density (A g^{-1})	Capacity (mAh g^{-1})	Cycling life	Ref.
Ect	7.56	10	140.2	~100%, 60,000 cycles	This work
BE-HEI	9.7	2	122.2	50.0%, 50,000 cycles	6
Zn-PCA	3	10	162.7	87.0%, 30,000 cycles	7
MeOH–TI	1.2	10	115	95.0%, 20,000 cycles	8
LA133	7.82	2	129.44	80.9%, 2,700 cycles	9
PNC-1000	6	1	170	89.0%, 10,000 cycles	10
I_2/OSTC	4	1	153	85.0%, 10,000 cycles	11
PC@Fe_2N-4/I_2	4.5	2	153	~86.0%, 20,000 cycles	12
Zn-CCS	3	2	115	~90.0%, 15,000 cycles	13
NiSAs-HPC	1	10	108	~91.5%, 40,000 cycles	14
M9	1.2	2	161.9	~92.5%, 10,000 cycles	15
ZT-12/NS-20	6.5	1	133	~78.2%, 5,000 cycles	16
Co@AC	1	1	112.3	68.0%, 1,000 cycles	17
KHP	2	10	113.8	~75.8%, 8,800 cycles	18
c-CNFs	13.9	2	130.5	98.7%, 4,000 cycles	19
Z@M-Zn	6	1	120	86.1%, 2400 cycles	20

Table S2 Comparison of additive prices and cycle life of this work with representative Zn–I_2 battery system reported recently

Strategies	Cycling life	Price (USD kg^{-1})	Supplier	Ref.	Price source
Ect	60000	498	Hubei Hongjing Chemical Co., Ltd.	This work	https://www.chemicalbook.com/SupplyInfo_481044.htm
TMSI	6500	360.11	TCI Shanghai	21	https://www.tcichemicals.com/CN/zh/p/T1056
BMMImTFSI	3500	1963	Macklin Inc.	22	https://www.macklin.cn/products/B857249
BE-HEI	50000	270.04	ACMEC	6	https://www.acmec-e.com/product/h583600
BMIS	15000	5364.7	ACMEC	23	https://www.acmec-e.com/product/b933200
EMIM	18000	842.57	Shanghai Amole Biotechnology Co., Ltd.	24	https://www.amole.com.cn/product/PNOa218569.html
RSC	17000	48.3	Macklin Inc.	25	https://www.macklin.cn/products/R817302
KHP	9000	22.7	Shanghai Kanglang Biotechnology Co., Ltd.	18	https://www.chemicalbook.com/SupplyInfo_520876.htm
CHS	16000	665.86	Shanghai Amole Biotechnology Co., Ltd.	26	https://www.amole.com.cn/product/PNOA144965.html

Table S3 Comparison of the practical application potential of this work with representative Zn–I_2 battery system reported recently

Strategies	Areal Capacity (mAh cm^{-2})	Zn utilization (%)	Cycling life	Ref.
Ect	6.95	80	80.0%, 310 cycles	This work
Ect	7.1	65	80.0%, 1,060 cycles	This work
cCNF/AC	0.94	8.47	~89.8%, 400 cycles	27
ZT-12/NS-20	0.69	20	~94.1%, 600 cycles	16
MX-AB@I	4	78.7	94.4%, 200 cycles	28
PAH-PCH	2.77	33.3	76.9%, 100 cycles	29
AHE	1.5	20	~87.1%, 300 cycles	30
BBAS	2.33	33	87.1%, 350 cycles	31
ZS-EAc	1.46	33	~88.0%, 200 cycles	32
Dowex+Fe-SCNT/GF	3.6	20	~85.7%, 800 cycles	33
CCH	1.5	35.7	~100%, 150 cycles	34
Sb_2O_3@Zn	3.9	14.7	~93.5%, 100 cycles	35
ZSO+ACES−K(0.5)	5.7	9.7	78.8%, 600 cycles	36
ZSO+CsI	2.26	17.8	54.8%, 100 cycles	37
BMIS	3.97	82	94.1%, 150 cycles	23
SP-$ZnCl_2$	3.47	20	95.0%, 1,000 cycles	38

Supplementary References

1 M. J. Frisch, G. W. Trucks, H. B. Schlegel, G. E. Scuseria, M. A. Robb, J. R. Cheeseman, G. Scalmani, V. Barone, G. A. Petersson, H. Nakatsuji, X. Li, M. Caricato, A. V. Marenich, J. Bloino, B. G. Janesko, R. Gomperts, B. Mennucci, H. P. Hratchian, J. V. Ortiz, A. F. Izmaylov, J. L. Sonnenberg, D. Williams-Young, F. Ding, F. Lipparini, F. Egidi, J. Goings, B. Peng, A. Petrone, T. Henderson, D. Ranasinghe, V. G. Zakrzewski, J. Gao, N. Rega, G. Zheng, W. Liang, M. Hada, M. Ehara, K. Toyota, R. Fukuda, J. Hasegawa, M. Ishida, T. Nakajima, Y. Honda, O. Kitao, H. Nakai, T. Vreven, K. Throssell, J. A. Montgomery Jr., J. E. Peralta, F. Ogliaro, M. J. Bearpark, J. J. Heyd, E. N. Brothers, K. N. Kudin, V. N. Staroverov, T. A. Keith, R. Kobayashi, J. Normand, K. Raghavachari, A. P. Rendell, J. C. Burant, S. S. Iyengar, J. Tomasi, M. Cossi, J. M. Millam, M. Klene, C. Adamo, R. Cammi, J. W. Ochterski, R. L. Martin, K. Morokuma, O. Farkas, J. B. Foresman and D. J. Fox, Gaussian 16 (Revision C.01), Gaussian Inc., Wallingford, CT, 2016.

2 A. D. Becke, *J. Chem. Phys.*, 1993, **98**, 5648–5652.

3 F. Weigend and R. Ahlrichs, *Phys. Chem. Chem. Phys.*, 2005, **7**, 3297.

4 S. Grimme, J. Antony, S. Ehrlich and H. Krieg, *J. Chem. Phys.*, 2010, **132**, 154104.

5 E. R. Johnson and A. D. Becke, *J. Chem. Phys.*, 2005, **123**, 024101.

6 J. Chen, G. Ou, P. Liu, W. Fan, B. Li, Z. Hu, Z. Wen, Y. Zhang, Y. Tang, X. Liu, M. Ye and C. C. Li, *Angew. Chem. Int. Ed.*, 2025, **64**, e202414166.

7 F. Wang, W. Liang, X. Liu, T. Yin, Z. Chen, Z. Yan, F. Li, W. Liu, J. Lu, C. Yang and Q.-H. Yang, *Adv. Energy Mater.*, 2024, **14**, 2400110.

8 W. Deng, R. Feng and X. Wang, *Energy Environ. Sci.*, 2024, **17**, 8643–8657.

9 K. Wang, H. Li, Z. Xu, Y. Liu, M. Ge, H. Wang, H. Zhang, Y. Lu, J. Liu, Y. Zhang, Y. Tang and S. Chen, *Adv. Energy Mater.*, 2024, **14**, 2304110.

10 T. Liu, H. Wang, C. Lei, Y. Mao, H. Wang, X. He and X. Liang, *Energy Storage Mater.*, 2022, **53**, 544–551.

11 M. Chen, W. Zhu, H. Guo, Z. Tian, L. Zhang, J. Wang, T. Liu, F. Lai and J. Huang, *Energy Storage Mater.*, 2023, **59**, 102760.

12 Q. Chen, S. Chen, J. Ma, S. Ding and J. Zhang, *Nano Energy*, 2023, **117**, 108897.

13 Z. Hu, X. Wang, W. Du, Z. Zhang, Y. Tang, M. Ye, Y. Zhang, X. Liu, Z. Wen and C. C. Li, *ACS Nano*, 2023, **17**, 23207–23219.

14 L. Ma, G. Zhu, Z. Wang, A. Zhu, K. Wu, B. Peng, J. Xu, D. Wang and Z. Jin, *Nano Lett.*, 2023, **23**, 5272–5280.

15 X. Guo, H. Xu, Y. Tang, Z. Yang, F. Dou, W. Li, Q. Li and H. Pang, *Adv. Mater.*, 2024, **36**, 2408317.

16 R. Wang, Z. Liu, J. Wan, X. Zhang, D. Xu, W. Pan, L. Zhang, H. Li, C. Zhang and Q. Zhang, *Adv. Energy Mater.*, 2024, **14**, 2402900.

17 L. Zhu, X. Guan, Y. Fu, Z. Zhang, Y. Li, Q. Mai, C. Zhang, Z. Yuan, Y. Wang, P. Li, H. Li, D. Su, B. Jia, H. Yu, Y. Sun and T. Ma, *Adv. Funct. Mater.*, 2024, **34**, 2409099.

18 H. Fu, S. Huang, T. Wang, J. Lu, P. Xiong, K. Yao, J. S. Byun, W. Li, Y. Kim and H. S. Park, *Adv. Mater.*, 2025, **37**, 2411686.

19 H. Qu, W. Guo, W. Li, L. Shao, Y. Chen, S. Su, L. Hang and G. Jiang, *Appl. Surf. Sci.*, 2025, **686**, 162180.

20 J. Liu, S. Chen, W. Shang, J. Ma and J. Zhang, *Adv. Funct. Mater.*, 2025, **35**, 2422081.

21 X. Liao, Z. Zhu, Y. Liao, K. Fu, Y. Duan, L. Lv, L. Wu, W. Wang, X. He, K. Yang, P. Tian, W. Cai, C. Zhao,

H. Tang and L. He, *Adv. Energy Mater.*, **14**, 2402306.

22 L. Zhao, D. Yin, Y. Zhang, B. Li, S. Wang, X. Cui, J. Feng, N. Gao, X. Liu, S. Ding and H. Zhao, *Energy Environ. Sci.*, 2025, **18**, 8952–8963.

23 H. Wu, J. Hao, S. Zhang, Y. Jiang, Y. Zhu, J. Liu, K. Davey and S.-Z. Qiao, *J. Am. Chem. Soc.*, 2024, **146**, 16601–16608.

24 T. Xiao, J.-L. Yang, B. Zhang, J. Wu, J. Li, W. Mai and H. J. Fan, *Angew. Chem. Int. Ed.*, 2024, **63**, e202318470.

25 Z. Chen, X. Gao, L. Shan, Q. Fu, Z. Xing, P. Rao, Z. Kang, X. Shi, W. Zhang and X. Tian, *Energy Environ. Sci.*, 2025, **18**, 8768–8779.

26 T. Su, W. Ren, M. Xu, P. Xu, J. Le, X. Ji, H. Dou, R. Sun and Z. Chen, *Adv. Energy Mater.*, **14**, 2401737.

27 Z. Li, W. Cao, T. Hu, Y. Hu, R. Zhang, H. Cui, F. Mo, C. Liu, C. Zhi and G. Liang, *Angew. Chem. Int. Ed.*, 2024, **136**, e202317652.

28 D. Li, Y.-J. Zhu, L. Cheng, S. Xie, H.-P. Yu, W. Zhang, Z. Xu, M.-G. Ma and H. Li, *Adv. Energy Mater.*, 2025, **15**, 2404426.

29 J.-L. Yang, Z. Yu, J. Wu, J. Li, L. Chen, T. Xiao, T. Xiao, D.-Q. Cai, K. Liu, P. Yang and H. J. Fan, *Adv. Mater.*, 2023, **35**, 2306531.

30 Q. Liu, Z. Yu, K. Fan, H. Huang and B. Zhang, *ACS Nano*, 2024, **18**, 22484–22494.

31 Y. Liu, F. Li, J. Hao, H. Li, S. Zhang, J. Mao, T. Zhou, R. Wang, L. Zhang and C. Zhang, *Adv. Funct. Mater.*, 2024, **34**, 2400517.

32 T. Xiao, J.-L. Yang, B. Zhang, J. Wu, J. Li, W. Mai and H. J. Fan, *Angew. Chem. Int. Ed.*, 2024, **63**, e202318470.

33 Y. Kang, G. Chen, H. Hua, M. Zhang, J. Yang, P. Lin, H. Yang, Z. Lv, Q. Wu, J. Zhao and Y. Yang, *Angew. Chem. Int. Ed.*, 2023, **62**, e202300418.

34 J. L. Yang, T. Xiao, T. Xiao, J. Li, Z. Yu, K. Liu, P. Yang and H. J. Fan, *Adv. Mater.*, 2024, **36**, e2313610.

35 P. Xiao, Y. Wu, K. Liu, X. Feng, J. Liang, Y. Zhao, C. Wang, X. Xu, T. Zhai and H. Li, *Angew. Chem. Int. Ed.*, 2023, **135**, e202309765.

36 G. Qu, Y. Zhao, C. Li, Y. Zhai, Y. Kong, X. He, L. Kong, C. Wang, M. Chen, K. Song, Z. Liu and L. Xu, *Angew. Chem. Int. Ed.*, 2025, **64**, e202422036.

37 Y. Deng, Z. Xiao, D. Liu, S. Wu, J. Zou, Z. Jiang and Y. Li, *J. Alloys Compd.*, 2025, **1012**, 178424.

38 S.-J. Zhang, J. Hao, H. Wu, Q. Chen, C. Ye and S.-Z. Qiao, *Adv. Mater.*, 2024, **36**, 2404011.